DEVELOPMENTAL CELL, VOLUME *21*

SUPPLEMENTAL INFORMATION

Structural and Functional Studies of LRP6 Ectodomain Reveal a Platform for Wnt Signaling

Shuo Chen, Doryen Bubeck, Bryan T. MacDonald, Wen-Xue Liang, Jian-Hua Mao, Tomas Malinauskas, Oscar Llorca, A. Radu Aricescu, Christian Siebold, Xi He, and E. Yvonne Jones

INVENTORY OF SUPPLEMENTAL INFORMATION

Supplemental Data

Figure S1 is related to Figure 1 and accompanies the text describing the crystal structure of $LRP6_{P3E3P4E4}$. It also supports the results from cellular assays probing the inter-PE pair interfaces.

Figure S2 is related to Figure 2 and illustrates the quality of the $LRP6_{ECD}$ reconstruction. It shows the resolution of the map and the angular distribution of the raw images. In addition, it demonstrates an agreement between projections of the map and averages of aligned particles.

Figure S3 is related to Figure 3 and presents metrics of evaluating the $LRP6_{ECD}$–Mesd reconstruction. Similar to Figure S2, it describes the resolution of the reconstruction and confirms that the raw images comprise of a wide range of orientations. The consistency of the reconstruction with the raw data is also assessed.

Figure S4 is related to Figure 4 and details the structural characteristics of the LRP6 residues implicated in Wnt3a binding and signaling. It also demonstrates that the mutations of these residues do not affect LRP6–Mesd interaction or Wnt1 signaling through LRP6.

Figure S5 is related to Figure 5 and illustrates the surface plasmon resonance (SPR) sensograms and nonlinear regression analysis of the outputs studying the interaction between $LRP6_{P3E3P4E4}$ constructs and Dkk1.

Table S1 is related to Figure 6 and lists the available information and proposed structural basis of disease-associated LRP mutations and mutations from mouse models.

Supplemental Experimental Procedures

Supplemental References

SUPPLEMENTAL DATA

Figure S1, related to Figure 1.

A

Figure S1 (continued)

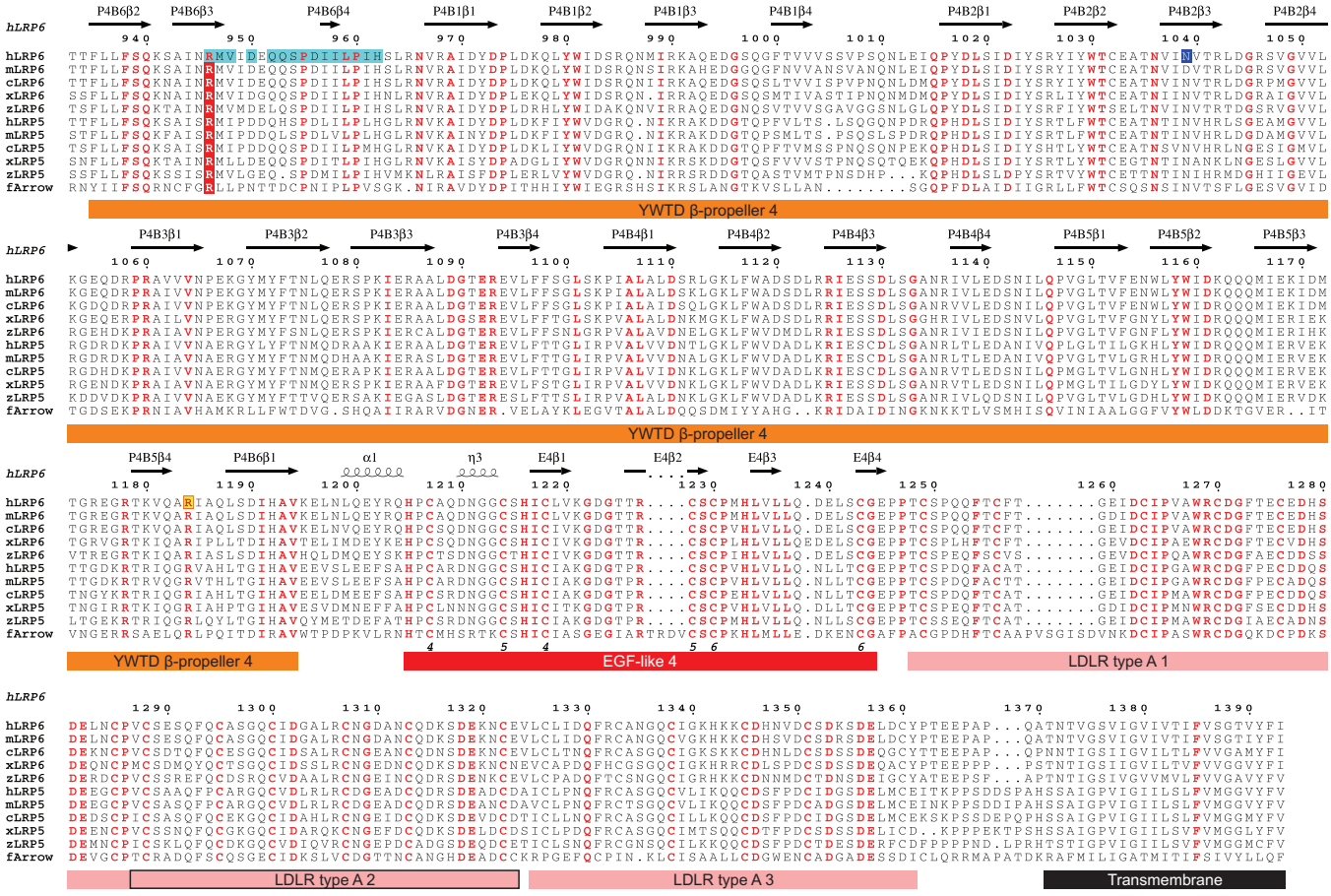

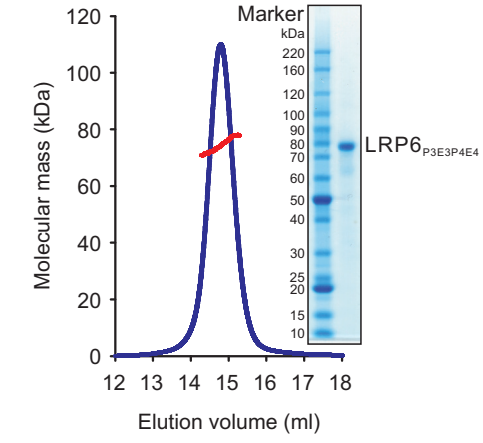

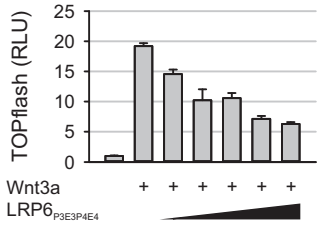

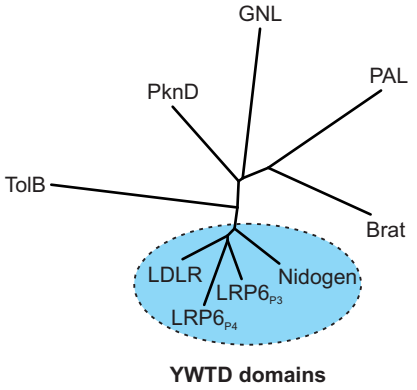

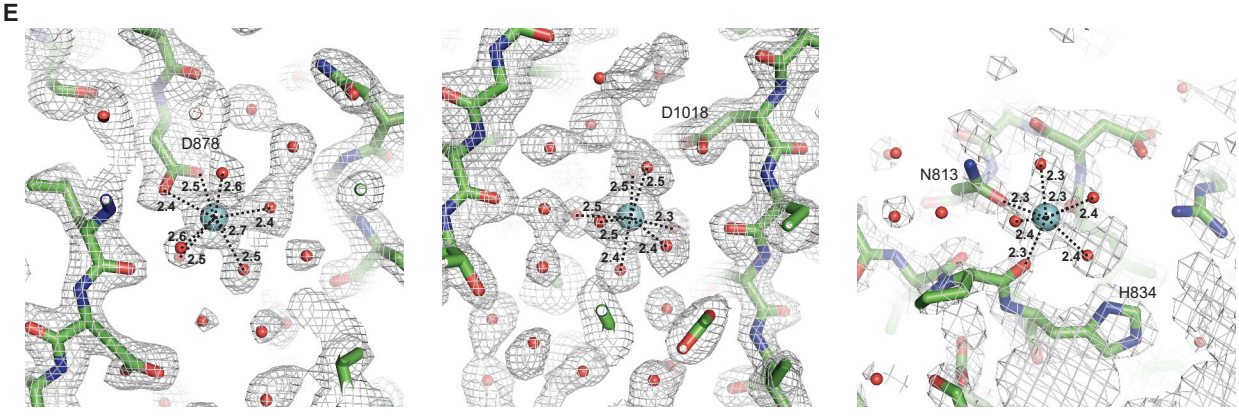

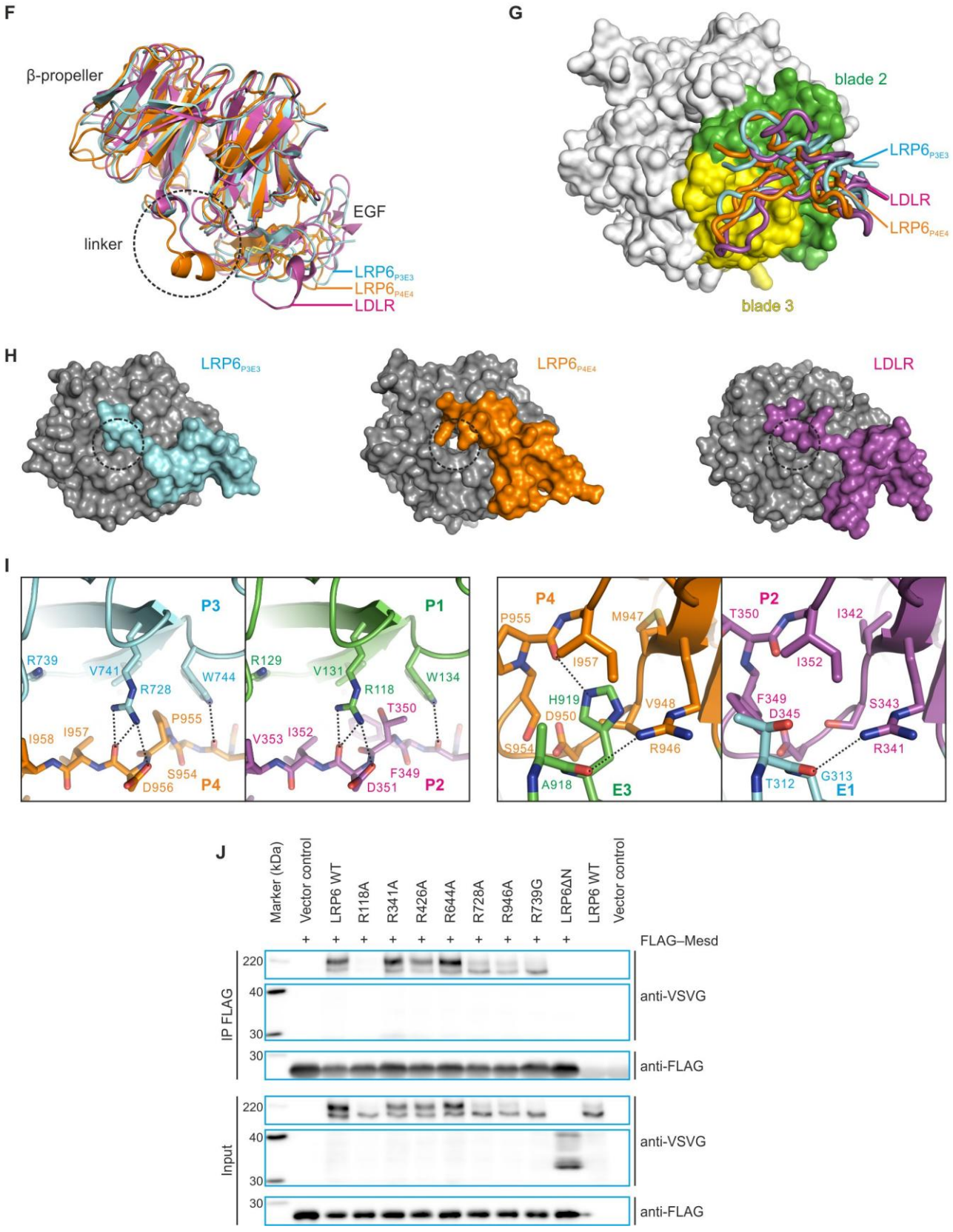

Figure S1, related to Figure 1. Structural and Functional Analyses of LRP6$_{P3E3P4E4}$

(A) Sequence alignment of vertebrate LRP6 and LRP5 and *Drosophila* Arrow. The amino acid sequences of human (abbreviated as h), mouse (m), chicken (c), *Xenopus laevis* (x) and zebrafish (z) LRP6 and LRP5 and *Drosophila* (f) Arrow extracellular domains were aligned using ClustalW2 (Larkin et al., 2007) and formatted with ESPript (Gouet et al., 1999). Evolutionarily conserved residues are in red. Residues at the inter-PE pair interface observed in the crystal structure are highlighted in cyan. Residues important for Wnt3a signaling are highlighted in yellow while those critical for Dkk1 inhibition are boxed in red. Arginines mutated to probe the inter-PE pair interfaces are highlighted in red. Domain structures are displayed below the alignment and

secondary structure definitions for $LRP6_{P3E3P4E4}$ above the alignment. Disulfide bridges are numbered below the sequences. Following crystal structure refinement, electron density for *N*-linked glycans is clear at residues 692, 859, 926 and 1039 (highlighted in blue). Predicted *N*-linked glycosylation sites outside $LRP6_{P3E3P4E4}$ are boxed in blue.

(B) Multi-angle light scattering indicates an experimental molecular mass (red line) of 74.4 ± 2.4 kDa for $LRP6_{P3E3P4E4}$ (blue line; elution profile, axis not shown) as observed by SDS–PAGE (inset) and in agreement with the calculated molecular mass for a monomer (76.1 kDa).

(C) Purified $LRP6_{P3E3P4E4}$ inhibits Wnt3a activity in a dose-dependent manner in Wnt-responsive TOPflash luciferase assay. Wnt3a (R&D 5036-WNP/CF) was used at 8 nM to activate signaling. $LRP6_{P3E3P4E4}$ doses were from 0.125 μM to 2 μM. RLU, relative light unit. Error bars represent standard error of the mean (SEM).

(D) Structure-based phylogenetic analysis of YWTD domains and related structures. The structures of the two YWTD β-propeller domains from $LRP6_{P3E3P4E4}$ and those from the top seven structural hits, including nidogen (Takagi et al., 2003) (PDB code 1NPE), LDLR (Jeon et al., 2001) (PDB code 1IJQ); the Brain Tumour (Brat) protein (Edwards et al., 2003) (PDB code 1Q7F), TolB (Loftus et al., 2006) (PDB code 2IVZ), *Mycobacterium tuberculosis* PknD (Good et al., 2004) (PDB code 1RWI), peptidyl-α-hydroxyglycine α-amidating lyase (PAL) (Chufan et al., 2009) (PDB code 3FW0) and a gluconolactonase (GNL) (Chen et al., 2008) (PDB code 3DR2), from the Dali server (Holm and Rosenstrom, 2010), using the structure of $LRP6_{P3}$ as a search probe, were superimposed and a pairwise distance matrix was constructed based on structural similarity with the program SHP (Stuart et al., 1979) and converted into a tree representation with the PHYLIP package (http://evolution.genetics.washington.edu/phylip.html). Structures of YWTD domains cluster together, away from other related β-propellers.

(E) Ca^{2+}-binding sites. A composite omit map was generated to the resolution of 1.9 Å using Phenix to reduce model bias and the resulting electron density around the three Ca^{2+} ion (the cyan sphere in the middle of each panel)-binding sites (in the central channel of P3, left panel; in the central channel of P4, middle panel; on the top surface of P3, right panel) is shown (contoured at 1.5 σ). Carbon, nitrogen and oxygen atoms are colored in green, blue and red, respectively.

(F) Cartoon representation of structures of YWTD β-propeller–EGF domain pairs ($LRP6_{P3E3}$, cyan; $LRP6_{P4E4}$, orange; LDLR, magenta) superposed based on the β-propeller domains. The PE pairs share a common interdomain organization while the linkers (in the dotted circle) between a β-propeller and its following EGF may vary.

(G) The EGF-like domains (shown as tubes color-coded as in (F)) of the PE pairs pack against an area on the YWTD β-propellers (surface representation) comprising the second (green) and third (yellow) blades.

(H) The entrance to the central channel of the β-propeller (in dotted circles in the middle of the panels) is covered by the linkers connecting the β-propeller and the EGF in the cases of $LRP6_{P3E3}$ and LDLR but exposed in $LRP6_{P4E4}$.

(I) Residues critical at the P3E3–P4E4 interface at their equivalent positions at the P1E1–P2E2 interface. Arg728 on P3 and its environment as in the crystal structure is compared with the model of corresponding Arg118 on P1 (left panels). Residues in the proximity of Arg118 are substituted for those around Arg728 based on the sequence alignment of P1E1P2E2 and P3E3P4E4 manually in Coot (Emsley and Cowtan, 2004). Similarly, Arg946 is compared with Arg341 (right panels).

(J) Co-immunoprecipitations suggested that mutations at the P3E3–P4E4 interface and at corresponding positions of other potential inter-pair interfaces of LRP6 did not alter its interaction with Mesd except for R118A. LRP6ΔN, an LRP6 mutant lacking most of the extracellular domain (Tamai et al., 2004), served as a negative control.

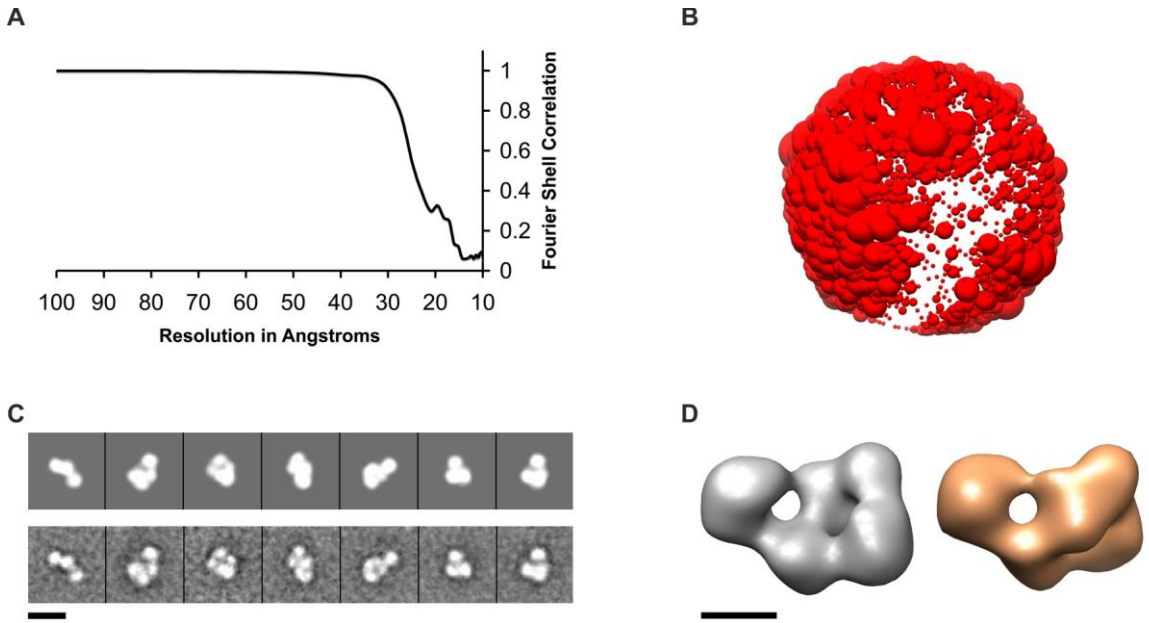

Figure S2, related to Figure 2. Three-Dimensional Reconstruction of LRP6$_{ECD}$ at 25-Å Resolution

(A) The final resolution of the LRP6$_{ECD}$ reconstruction was assessed using the Fourier shell correlation with a cut-off of 0.5.

(B) The angular distribution of particle orientations was plotted in three dimensions using Chimera. Spheres represent unique orientations, where the size of the sphere is proportional to the number of particles assigned to a given set of angles.

(C) Two-dimensional projections of the LRP6$_{ECD}$ reconstruction (top panel) were compared with averages of raw images (bottom panel). Representative orientations are shown.

(D) Two possible hands of the LRP6$_{ECD}$ reconstruction (grey and orange surfaces) are visualized. The reconstruction in grey is also depicted in Figure 2. Scale bars, 140 Å (C) and 50 Å (D).

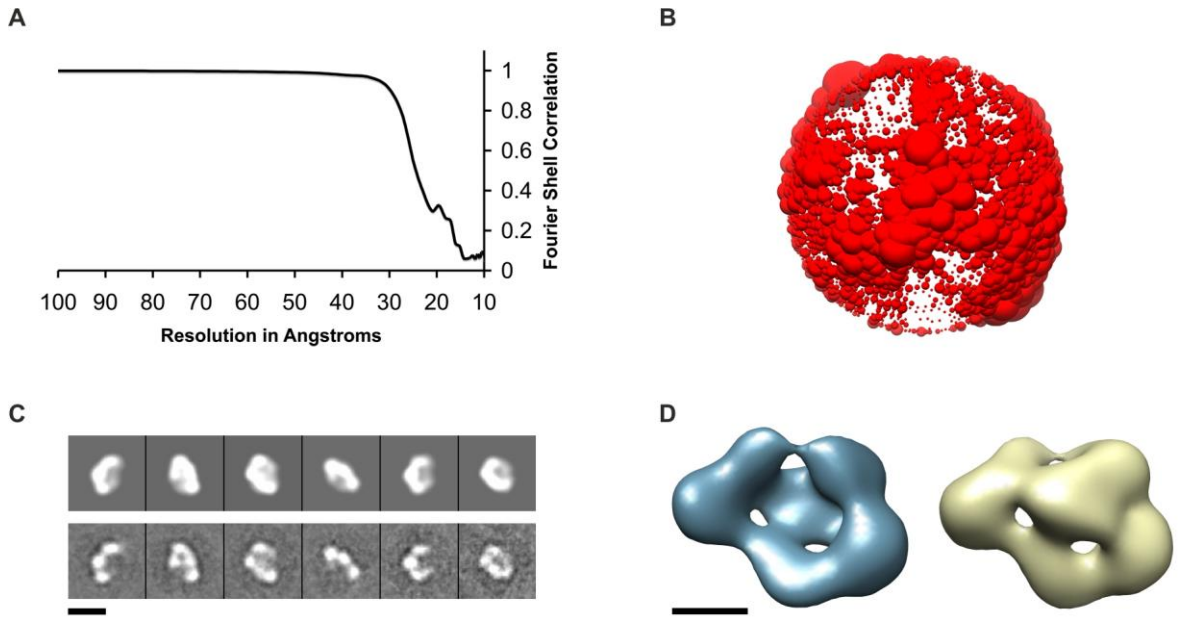

Figure S3, related to Figure 3. Electron Microscopy Reconstruction of the Negatively Stained LRP6$_{ECD}$–Mesd Complex

(A) Using the Fourier shell correlation at 0.5, the resolution of the map was determined to be 26 Å.

(B) Complexes lie in diverse orientations on the EM grid. The distribution of the angular assignments was plotted using Chimera. Each sphere corresponds to a unique set of angles and the diameter of the sphere correlates with the number of particles assigned to that orientation.

(C) Consistency of the LRP6$_{ECD}$–Mesd reconstruction with the raw images was assessed by comparing two-dimensional projections (top panel) with corresponding class averages (bottom panel). Typical averages illustrating a range of orientations are shown.

(D) The two alternative hands of the LRP6$_{ECD}$–Mesd reconstruction are represented as blue and yellow surfaces, where the blue surface is also shown in Figure 3. Scale bars, 140 Å (C) and 50 Å (D).

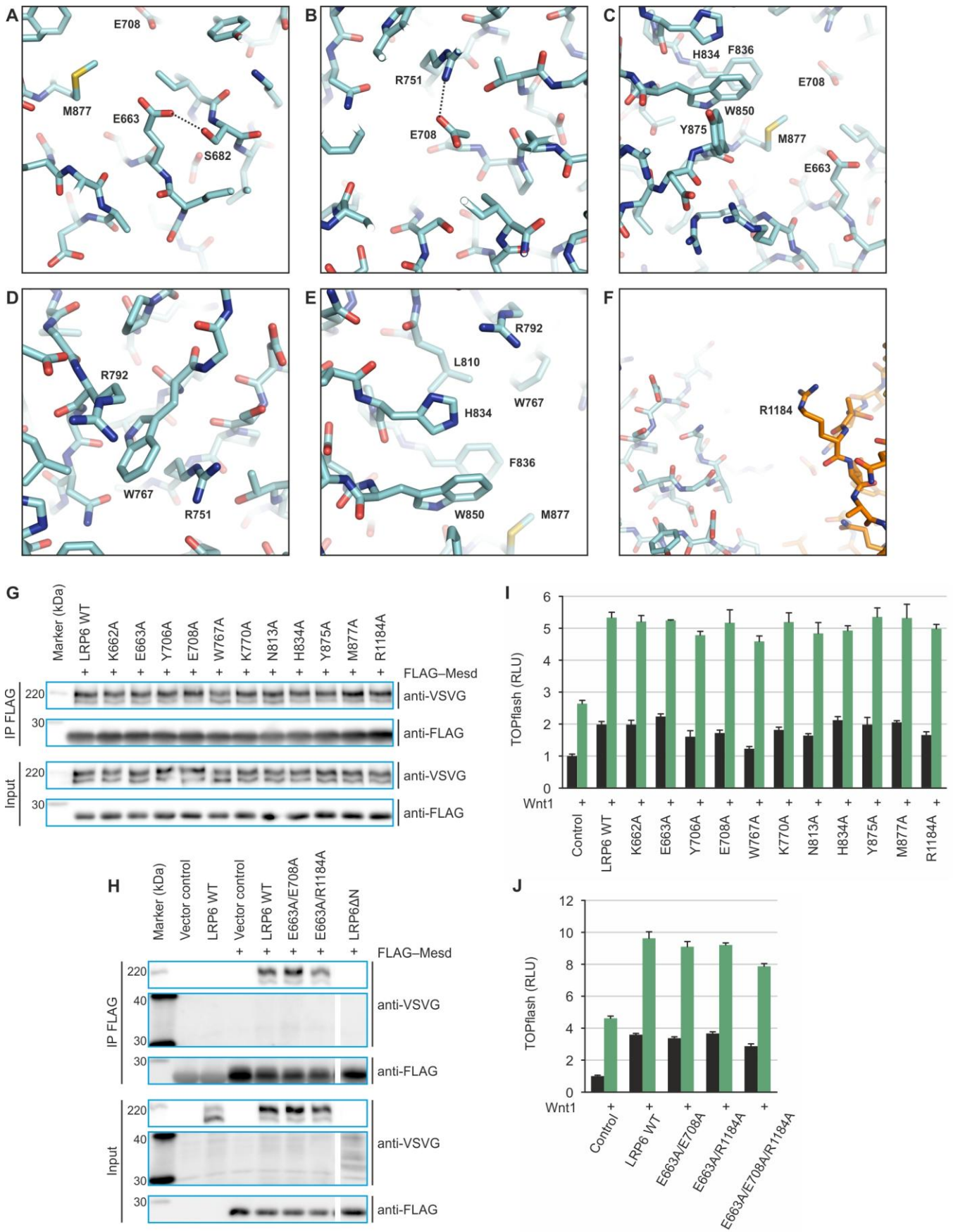

Figure S4, related to Figure 4. Structural Characteristics of LRP6 Residues Implicated in Wnt3a Binding and Signaling

(A)–(F) Close-up views of LRP6 residues (represented as sticks), Glu663 (A), Glu708 (B), Tyr875 and Met877 (C), Trp767 (D), His834 (E), and Arg1184 (F), whose mutations affected Wnt3a binding and signaling. Nitrogen,

oxygen, and sulfur atoms are colored in blue, red, and yellow, respectively. Carbon atoms of P3 residues are in cyan whereas those of P4 residues in orange.

(G and H) Mutations on the top faces of P3 and P4 of LRP6 did not affect its interaction with Mesd. The LRP6 mutants reach the cell surface at comparable levels except the one carrying W767A. The Mesd co-immunoprecipitation experiment for the single residue mutants was performed in parallel with the interface mutants, see Figure S1J for control lanes.

(I and J) LRP6 single mutants (I) and double mutants (J) transduced Wnt1 signaling at similar levels in luciferase reporter assay. The LRP6 triple mutant exhibited mild defect in Wnt1 signaling (J). Error bars represent standard deviations.

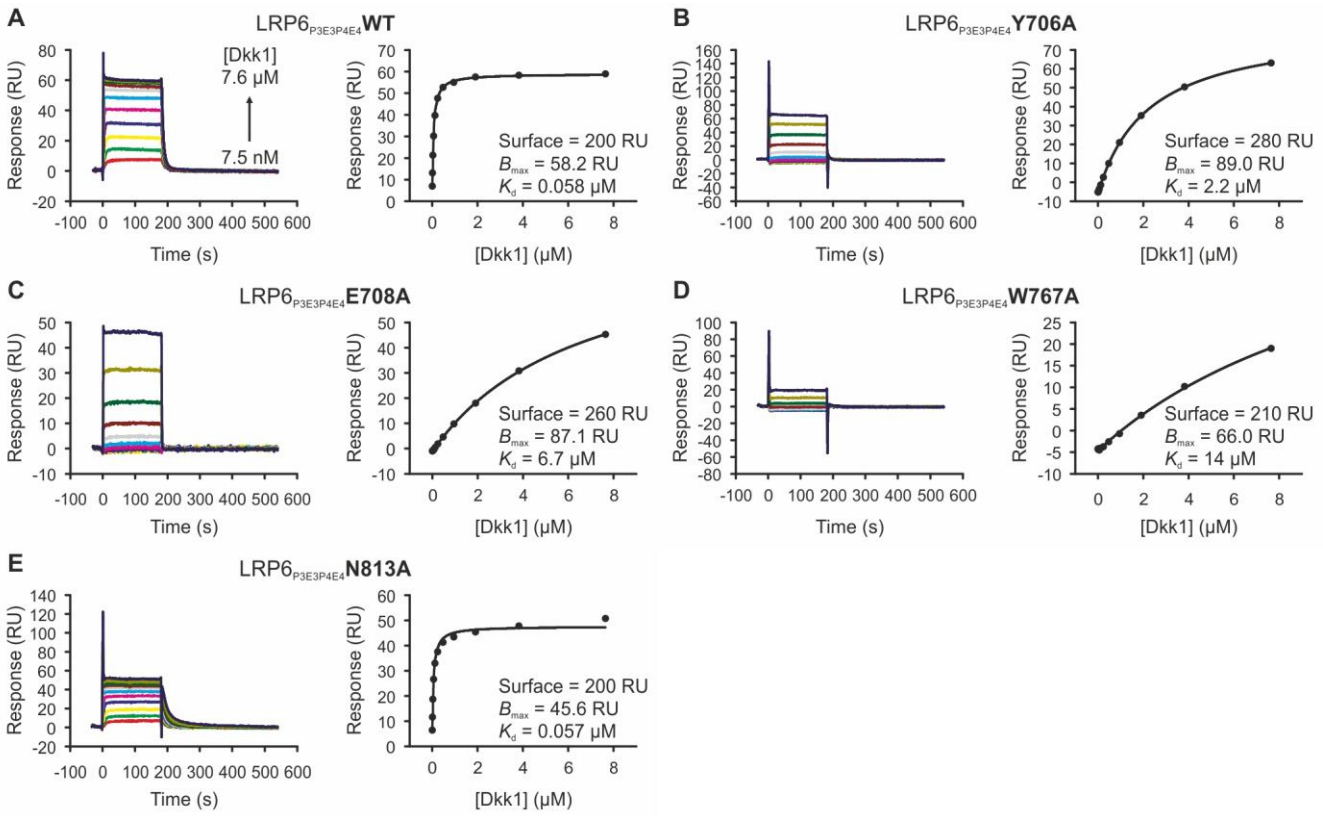

Figure S5, related to Figure 5. Diminished Wnt Inhibition by Dkk1 Correlates with Reduced Binding to LRP6 Mutants

SPR sensograms (left panels) and nonlinear regression assuming the Langmuir adsorption model (right panels) are shown. In the sensograms, colors denote concentrations of analyte (Dkk1) used (from 7.5 nM to 7.6 μM). The amounts of ligands immobilized onto sensor chip surfaces, and B_{max} and K_d values (defined in Supplemental Experimental Procedures) obtained are indicated.

(A) Dkk1 binds to WT LRP6$_{P3E3P4E4}$ with a K_d of 0.058 μm.

(B, C and D) Relative to WT LRP6$_{P3E3P4E4}$, mutations Y706A (B), E708A (C) and W767A (D) lead to more than 30-, 100- and 200-fold drop in their respective affinities to bind Dkk1, consistent with diminished inhibition by Dkk1.

(E) The mutation N813A in LRP6$_{P3E3P4E4}$ has negligible effect on Dkk1 binding, in agreement with the inhibition of its corresponding full-length mutant by Dkk1.

Table S1, related to Figure 6. Potential Structural Consequences of Disease-Associated LRP Mutations and Mutations from Mouse Models

Mutation	Characterization	References	Location	Potential structural consequences
LRP6				
Coronary artery disease (loss of function)				
R611C	Diminished WNT signaling	(Mani et al., 2007)	E2; next to Cys612 that is involved in a disulfide bond	Impaired folding or stability of the EGF domain
Late-onset Alzheimer's disease and low bone mass (variant; loss of function)				
I1062V	Diminished WNT signaling	(De Ferrari et al., 2007)	P4B3β1	Compromised folding or stability of the β-propeller domain
LRP5				
Osteoporosis pseudoglioma (OPPG; loss of function)				
D203N	Not characterized	(Ai et al., 2005a)	P1B4β1	Impaired folding or stability of the β-propeller domain
T244M	Impaired traffic; diminished WNT and Norrin signaling	(Ai et al., 2005a)	P1B5β1	Impaired folding or stability of the β-propeller domain
S307F	Not characterized	(Ai et al., 2005a)	E1; next to Cys306 that is involved in a disulfide bond	Impaired folding or stability of the EGF domain
R353Q	Not characterized	(Ai et al., 2005a)	P2B6β3	Impaired folding or stability of the β-propeller domain; and/or disrupted P1E1–P2E2 interface
S356L	Diminished WNT and Norrin signaling	(Ai et al., 2005a)	P2B6β3–P2B6β4 loop (bottom face)	Disrupted P1E1–P2E2 interface
A400E	Not characterized	(Ai et al., 2005a)	P2B1β3	Impaired folding or stability of the β-propeller domain; and/or disrupted P1E1–P2E2 interface
G404R	Impaired traffic; diminished WNT and Norrin signaling	(Ai et al., 2005a)	P2B1β3–P2B1β4 loop (bottom face)	Impaired folding or stability of the β-propeller domain; disrupted P1E1–P2E2 interface
T409A	Not characterized	(Streeten et al., 2008)	P2B1β4	Impaired folding or stability of the β-propeller domain; and/or disrupted P2E2–P3E3 interface
D434N	Impaired traffic; diminished WNT and Norrin signaling	(Ai et al., 2005a)	P2B2β2	Impaired folding or stability of the β-propeller domain
E460K	Not characterized	(Ai et al., 2005a)	P2B2β4–P2B3β1 loop (top face)	Impaired folding or stability of the β-propeller domain; and/or altered ligand binding
W478R	Not characterized	(Cheung et al., 2006)	P2B3β2–P2B3β3 loop (top face)	Impaired folding or stability of the β-propeller domain; and/or altered ligand binding
R494Q	Not characterized	(Gong et al., 2001)	P2B3β3–P2B3β4 loop (bottom face)	Impaired folding or stability of the β-propeller domain; and/or disrupted P2E2–P3E3 interface
W504C	Not characterized	(Cheung et al., 2006)	P2B3β4–P2B4β1 loop (top face)	Impaired folding or stability of the β-propeller domain; and/or altered ligand binding
G520V	Diminished WNT and Norrin signaling	(Ai et al., 2005a)	P2B4β2	Impaired folding or stability of the β-propeller domain; and/or altered ligand binding
N531A	Not characterized	(Barros et al., 2008)	P2B4β3	Impaired folding or stability of the β-propeller domain; and/or, less likely, altered ligand binding
R570W	Not characterized	(Gong et al., 2001)	P2B5β3	Impaired folding or stability of the β-propeller domain
D683N	Not characterized	(Ai et al., 2005a)	P3B1β1	Impaired folding or stability of the β-propeller domain
Y733H	Not characterized	(Ai et al., 2005a)	P3B2β2	Impaired folding or stability of the β-propeller domain
Familial exudative vitreoretinopathy (FEVR; loss of function)				
L145F	Not characterized	(Qin et al., 2005)	P1B2β4	Impaired folding or stability of the β-propeller domain; and/or disrupted P1–E1 interface
E441K	Not characterized	(Nikopoulos et al., 2010)	P2B2β3	Impaired folding or stability of the β-propeller domain; and/or disrupted P2E2–P3E3 interface
R444C	Diminished Norrin signaling	(Qin et al., 2005; Qin et al., 2008)	P2B2β3	Impaired folding or stability of the β-propeller domain; and/or disrupted P2–E2 interface
D511A	Not characterized	(Boonstra et al., 2009)	P2B4β1	Impaired folding or stability of the β-propeller domain
A522T	Diminished Norrin signaling	(Qin et al., 2005; Qin et al., 2008)	P2B4β2–P2B4β3 loop (top face)	Impaired folding or stability of the β-propeller domain; and/or altered ligand binding
T535M	Not characterized	(Qin et al., 2005)	P2B4β3–P2B4β4 loop (bottom face)	Impaired folding or stability of the β-propeller domain
G550R	Not characterized	(Downey et al., 2006)	P2B5β1	Impaired folding or stability of the β-propeller

				domain
R570Q	Diminished WNT and Norrin signaling	(Ai et al., 2005a; Jiao et al., 2004)	P2B5β3	Impaired folding or stability of the β-propeller domain
G610R	Not characterized	(Qin et al., 2005)	E2; close to Cys612 that is involved in a disulfide bond	Impaired folding or stability of the EGF domain
F617C	Not characterized	(Qin et al., 2005)	E2; next to Cys616 that is involved in a disulfide bond	Impaired folding or stability of the EGF domain
R752G	Diminished WNT signaling due to reduced cell surface expression	(Jiao et al., 2004); this study	P3B2β3–P3B2β4 loop (bottom face)	Disrupted P3E3–P4E4 interface
T798A	Not characterized	(Qin et al., 2005)	P3B3β4	Impaired folding or stability of the β-propeller domain; and/or, less likely, altered ligand binding
R805W	Not characterized	(Boonstra et al., 2009)	P3B3β4–P3B4β1 loop (top face)	Impaired folding or stability of the β-propeller domain; and/or altered ligand binding
N1121D	Not characterized	(Qin et al., 2005)	P4B4β1–P4B4β2 loop (bottom face)	Impaired folding or stability of the β-propeller domain
Y1168H	Diminished WNT and Norrin signaling	(Ai et al., 2005a; Toomes et al., 2004)	P4B5β2	Impaired folding or stability of the β-propeller domain
C1253F	Not characterized	(Nikopoulos et al., 2010)	E4; involved in a disulfide bond	Impaired folding or stability of the EGF domain
High bone mass (HBM; gain of function)				
D111Y	Diminished antagonist binding and inhibition	(Ai et al., 2005b; Semenov and He, 2006; Van Wesenbeeck et al., 2003)	P1B1β4–P1B2β1 loop (top face)	Diminished antagonist binding (directly involved)
R154M	Diminished SOST binding and inhibition	(Rickels et al., 2005; Semenov and He, 2006)	P1B2β4–P1B3β1 loop (top face)	Diminished antagonist binding (directly involved)
G171V	Impaired traffic; diminished antagonist binding and activity	(Ai et al., 2005b; Boyden et al., 2002; Little et al., 2002; Semenov and He, 2006)	P1B3β2–P1B3β3 loop (top face)	Diminished antagonist binding (directly involved)
G171R	Diminished DKK1 binding and inhibition	(Ai et al., 2005b; Van Wesenbeeck et al., 2003)	P1B3β2–P1B3β3 loop (top face)	Diminished antagonist binding (directly involved)
Deletion of Gly171 and Glu172	Diminished SOST and DKK1 inhibition	(Pangrazio et al., 2011)	P1B3β2–P1B3β3 loop (top face)	Diminished antagonist binding (directly involved)
N198S	Diminished SOST binding and inhibition	(Semenov and He, 2006)	P1B4β1	Diminished antagonist binding (indirectly involved)
A214T	Diminished antagonist binding and inhibition	(Ai et al., 2005b; Semenov and He, 2006; Van Wesenbeeck et al., 2003)	P1B4β2–P1B4β3 loop (top face)	Diminished antagonist binding (indirectly involved)
A214V	Diminished DKK1 binding and inhibition	(Ai et al., 2005b; Van Wesenbeeck et al., 2003)	P1B4β2–P1B4β3 loop (top face)	Diminished antagonist binding (indirectly involved)
A242T	Diminished DKK1 binding and inhibition	(Ai et al., 2005b; Van Wesenbeeck et al., 2003)	P1B5β1	Altered ligand binding (indirectly involved)
T253I	Diminished antagonist binding and inhibition	(Ai et al., 2005b; Semenov and He, 2006; Van Wesenbeeck et al., 2003)	P1B5β2	Diminished antagonist binding (indirectly involved)
M282V	Diminished DKK1 inhibition	(Balemans et al., 2007)	P1B5β4–P1B6β1 loop (top face)	Diminished antagonist binding (directly involved)
Lrp6				
***ringelschwanz* (*rs*; hypomorph)**				
R886W	Diminished Wnt signaling	(Kokubu et al., 2004)	P3–E3 linker	Impaired folding or stability of the β-propeller domain; and/or disrupted P3–E3 interface
***Crooked tail* (*Cd*; hypermorph)**				
G494D	Diminished Dkk1 inhibition	(Carter et al., 2005)	P2B4β1	Diminished antagonist binding (indirectly involved)
***Gwazi* (*Gw*; hypermorph)**				
D549G	Elevated Wnt signaling	(Fossat et al., 2011)	P2B5β2	Diminished antagonist binding (indirectly involved)

Mutations that potentially disrupt inter-pair interfaces are highlighted in cyan while those proposed to be possibly involved in altered ligand binding are yellow.

SUPPLEMENTAL EXPERIMENTAL PROCEDURES

Structure Determination and Refinement

Crystallization was carried out in sitting nanodrops (Walter et al., 2005). X-ray diffraction data were indexed and integrated with XDS (Kabsch, 2010) and then scaled using Scala (Evans, 2006). The structure was solved by molecular replacement in Phaser (McCoy et al., 2007) using the structure of LDLR β-propeller–EGF domain pair (Jeon et al., 2001) (Protein Data Bank accession code 1IJQ) as a search model. The structure was first automatically built by ARP/wARP (Perrakis et al., 1999) then iteratively built manually in Coot (Emsley and Cowtan, 2004), refined in Refmac (Murshudov et al., 1997) and validated with MolProbity (Chen et al., 2010). The Ramachandran plot of the structure shows 96.2% and 0% of its residues to be in the favored and the disallowed regions, respectively. Electrostatic potential was calculated using APBS (Baker et al., 2001), buried surface area using PISA (Krissinel and Henrick, 2007), and surface complementarity (Sc) using Sc (Lawrence and Colman, 1993). Structural figures were generated using PyMOL (Schrödinger), Consurf (Ashkenazy et al., 2010) and CorelDRAW (Corel).

Site-Directed Mutagenesis

VSVG-tagged full-length LRP6 (VSVG–LRP6) (MacDonald et al., 2008) and IgG-tagged LRP6 ectodomain (LRP6N–IgG) (Tamai et al., 2000) mutants were generated by QuikChange Lightning Site-Directed Mutagenesis Kit (Agilent Technologies) using the original constructs as the DNA templates. $LRP6_{P3E3P4E4}$ mutants were generated by two-step overlapping polymerase chain reactions (PCR) using Pyrobest polymerase (Takara) and cloned into pHL-AviTag3 resulting in a C-terminal AviTag for biotinylation (Aricescu et al., 2006).

Dual Luciferase Assay

Mammalian cell transfections were done in HEK293T (ATCC CRL-11268) cells using FuGENE HD (Roche) and performed in triplicate. Cells were plated at 1×10^5/ml in 24 well plates and transfected the following day with a total of 200 ng of DNA/well (50 ng TOPflash, 10 ng RL-TK, 5 or 10ng of full-length VSVG-tagged LRP6 (pCS2) and balanced with empty vector control (pCS2)). Polyclonal anti-VSVG (Sigma V4888) was used to detect VSVG–LRP6 by Western blot. 100 ng/well of Dkk1 (pCS2), 0.1 ng/well LNCX-Wnt1 or 0.1 ng/well LNCX-Wnt3a were used for co-expression assay (full details of all plasmids are available upon request). Results for Dkk1 inhibition were plotted using values first subtracted for baseline activity in the absence or presence of Dkk1, and were then normalized respective to each LRP6 construct plus Wnt as 100%. Wnt3a-conditioned medium was produced from L-Wnt3a cells (ATCC CRL-2647) and compared to control L cell (ATCC CRL-2648) conditioned medium. Dual luciferase reporter assays were performed as previously described (MacDonald et al., 2008). Representative results are shown from one of multiple independent experiments.

Cell Surface Biotinylation Assay

Hela cells (ATCC CCL-2) in 6-well plates were transfected with 1 μg of full-length VSVG–LRP6 (pCS2) and 1 μg Mesd (pCS2). Labeling of cell surface via biotinylation was performed as previously described (Semenov and He, 2006). Briefly, cells were washed with cold PBS and labeled for 30 min using 0.5 mg/ml Sulfo-NHS-SS-Biotin (Pierce). Free biotin was neutralized with 50 mM Tris-HCl (pH 8.8), 150 mM NaCl for 15 min, followed by 4 × cold PBS washes. Cells were lysed in PBS with 2% Triton X-100 and protease inhibitors (Roche). Cleared lysates were

diluted to 0.5% Triton X-100 for binding to Neutravidin-Sepharose (Pierce) at 4 °C. Samples were washed 4 × cold PBS + 0.5% Triton X-100; and loading buffer containing β-mercaptoethanol was used to reduce conjugated biotin. Polyclonal anti-VSVG (Sigma V4888) was used to detect the full-length VSVG–LRP6 receptors by Western blot. Endogenous human transferrin receptor (Invitrogen H68.4) was used as a cell surface receptor control. Results were verified using HEK293T cells.

Multi-Angle Light Scattering

MALS experiments were coupled to gel filtration chromatography. Properties of eluate from an analytical Superdex 200 10/300 GL column (GE Healthcare) were measured online using the DAWN HELEOS static light scattering (Wyatt Technology), the Optilab rEX refractive index (Wyatt Technology) and the 1200 UV (Agilent Technologies) detectors. Analytes had previously been purified by gel filtration chromatography. Data were analyzed using the ASTRA software package (Wyatt Technology).

Electron Microscopy and Image Processing

The purified $LRP6_{ECD}$ (2.5 µl of 30 µg/ml) and $LRP6_{ECD}$–Mesd complex (2.5 µl of 15 µg/ml) were applied to carbon-coated copper grids, which were glow-discharged for 10 seconds at 20 mA. Grids were negatively stained with 0.75% uranyl formate using the two-drop method (Ohi et al., 2004). Images were taken under low-dose conditions (~10 $e^-/Å^2$ per exposure) at a magnification of 72,500 on a JEOL JEM-1230 operated at 100 kV. Images were recorded on a 4k × 4k TemCam-F416 camera (TVIPS) and binned by a factor of 2, resulting in a pixel size of 4.56 Å/pixel. 6999 $LRP6_{ECD}$ and 7928 $LRP6_{ECD}$–Mesd windowed particles were each subjected to fourteen cycles of reference-free alignment using EMAN (Ludtke et al., 1999) and classified into 304 classes. A Gaussian blob (40 × 40 × 25 pixels) was used as reference to initiate the angular assignment of raw images. To minimize distortions of the structure, the initial models were used as references for Euler angular assignment of reference-free generated 2D class averages in EMAN. The improved models were then used as templates for the refinement of single particles. Structures were further refined until convergence using the projection matching algorithm in Xmipp (Scheres et al., 2008).

Fitting of Atomic Coordinates

A homology model of LRP6 residues 20–1244 based on the $LRP6_{P3E3P4E4}$ crystal structure was built using Modeller (Eswar et al., 2007). This single rigid-body was manually docked into the electron microscopy reconstruction and subjected to automated real-space refinement in Coot. Residues linking E2 and P3 (628–632) were removed. The model was subsequently refined as two rigid bodies (residues 20–627 and residues 633–1244) using Coot. Refined models were scored against the electron microscopy map using a real-space correlation coefficient computing using the Bsoft package (Heymann and Belnap, 2007). A homology model for the three LDLRA domains of $LRP6_{ECD}$ (residues 1249–1360) was based on the crystal structure of LDLR (residues 147–270) (Rudenko et al., 2002) (PDB code 1N7D). Density corresponding to this model was filtered to 25 Å resolution and placed manually into the remaining density of the $LRP6_{ECD}$ reconstruction using Chimera (Pettersen et al., 2004). The crystal structure of the mouse Mesd core domain (Collins and Hendrickson, 2011) (PDB code 3OFH; residues 98–183) was filtered to 25 Å and manually placed into the $LRP6_{ECD}$–Mesd reconstruction in Chimera. Although the handedness of the reconstructions was not empirically determined, the choice of hand does not affect the assignment of PE pairs to the perimeter of the planar $LRP6_{ECD}$ structure.

Co-immunoprecipitation Assays

For co-immunoprecipitation of LRP6 and Mesd, HEK293T cells in 12 well plates were transfected with 0.4 µg FLAG–Mesd and 0.4 µg VSVG–LRP6 full-length or non-Mesd binding control LRP6ΔN in pCS2. 36 h post transfection, cells were washed with PBS and lysed in 250 µl Triton Lysis Buffer (50 mM Tris-HCl (pH7.5), 150 mM NaCl, 1 mM EDTA, 1% Triton X-100, 10% glycerol, 5 mM DTT and Roche complete mini protease inhibitor cocktail) which was also used as a binding and wash buffer. For binding, 100 µl of input was combined with 500 µl additional Triton Lysis Buffer 10 µl of anti-FLAG M2 Affinity Gel (Sigma A2220) and incubated at 4 °C on a Nutator platform for 4 h. Samples were washed 4 × with 1 ml (10-min washes). Mesd–FLAG was detected using anti-FLAG M2 antibody (Sigma F3165). Full-length LRP6 was resolved on 7% gels, LRP6ΔN on 10% gels, FLAG–Mesd on 12% gels.

For co-immunoprecipitation of LRP6N and Wnt3a, LRP6N (Tamai et al., 2000) CM was produced from HEK293T cells transfected with LRP6N–IgG (pcDNA3) and Mesd (pCS2), at a ratio of 1:1 to increase LRP6N production. LDLRN–IgG (pCS2) was used as a control. For each sample, 1 ml of LRP6N CM was pre-cleared using Glutathione Sepharose 4B (GE Healthcare) for 1 h, then incubated with Protein G Sepharose 4 Fast Flow (GE Healthcare) to capture LRP6N–IgG onto beads. Prior to Wnt3a binding, LRP6N–IgG loaded Protein G beads were washed 3 × with 500 mM high salt PBS (pH 7.4) containing 1% CHAPS to remove non-specific proteins and equilibrated in PBS + 0.5% CHAPS (pH 7.4, 150 mM NaCl) binding buffer. An input of 100 ng of recombinant human Wnt3a (R&D 5036-WN) was used for LRP6N binding, followed by 4 × 10 min washes using PBS + 0.5% CHAPS. All binding and wash steps were conducted using a Nutator platform at 4 °C. Anti-Wnt3a (Cell Signaling C64F2) and anti-human IgG (CalBiochem 401445) were used for Western blot.

Surface Plasmon Resonance Binding Studies

SPR binding experiments were performed using a Biacore T100 (GE Healthcare) at 25 °C in 10 mM HEPES (pH 7.4), 150 mM NaCl, 0.005% (v/v) Surfactant P20. $LRP6_{P3E3P4E4}$ and its mutants were enzymatically biotinylated at a C-terminal AviTag using BirA (Avidity) and immobilized via streptavidin onto sensor chips. Similar amounts of the WT and the mutant proteins (~200 response units (RU)) were immobilized onto surfaces coupled with ~8,000 RU of streptavidin for comparison. Signals from experimental flow cells were corrected by subtraction from first a reference flow cell with only streptavidin coupled and then a blank cycle without an analyte in the solution. Values of dissociation constant (K_d) were obtained by nonlinear regression assuming the Langmuir adsorption model ($B = B_{max}C/(K_d + C)$, where variable B is the amount of bound analyte, variable C is the concentration of analyte in the solution before injection and constant B_{max} is the maximum amount of analyte that could bind). All analyses were carried out in BIAevaluation (GE Healthcare).

SUPPLEMENTAL REFERENCES

Ai, M., Heeger, S., Bartels, C.F., and Schelling, D.K. (2005a). Clinical and molecular findings in osteoporosis-pseudoglioma syndrome. Am. J. Hum. Genet. *77*, 741-753.

Ai, M., Holmen, S.L., Van Hul, W., Williams, B.O., and Warman, M.L. (2005b). Reduced affinity to and inhibition by DKK1 form a common mechanism by which high bone mass-associated missense mutations in LRP5 affect canonical Wnt signaling. Mol. Cell. Biol. *25*, 4946-4955.

Aricescu, A.R., Lu, W., and Jones, E.Y. (2006). A time- and cost-efficient system for high-level protein production in mammalian cells. Acta Crystallogr. D Biol. Crystallogr. *62*, 1243-1250.

Ashkenazy, H., Erez, E., Martz, E., Pupko, T., and Ben-Tal, N. (2010). ConSurf 2010: calculating evolutionary conservation in sequence and structure of proteins and nucleic acids. Nucl. Acids Res. *38*, W529-533.

Baker, N.A., Sept, D., Joseph, S., Holst, M.J., and McCammon, J.A. (2001). Electrostatics of nanosystems: application to microtubules and the ribosome. Proc. Natl. Acad. Sci. USA *98*, 10037-10041.

Balemans, W., Devogelaer, J.P., Cleiren, E., Piters, E., Caussin, E., and Van Hul, W. (2007). Novel LRP5 missense mutation in a patient with a high bone mass phenotype results in decreased DKK1-mediated inhibition of Wnt signaling. J. Bone Miner. Res. *22*, 708-716.

Barros, E.R., Dias da Silva, M.R., Kunii, I.S., and Lazaretti-Castro, M. (2008). Three years follow-up of pamidronate therapy in two brothers with osteoporosis-pseudoglioma syndrome (OPPG) carrying an LRP5 mutation. J. Pediatr. Endocrinol. Metab. *21*, 811-818.

Boonstra, F.N., van Nouhuys, C.E., Schuil, J., de Wijs, I.J., van der Donk, K.P., Nikopoulos, K., Mukhopadhyay, A., Scheffer, H., Tilanus, M.A., Cremers, F.P., and Hoefsloot, L.H. (2009). Clinical and molecular evaluation of probands and family members with familial exudative vitreoretinopathy. Invest. Ophthalmol. Vis. Sci. *50*, 4379-4385.

Boyden, L.M., Mao, J., Belsky, J., Mitzner, L., Farhi, A., Mitnick, M.A., Wu, D., Insogna, K., and Lifton, R.P. (2002). High bone density due to a mutation in LDL-receptor-related protein 5. N. Engl. J. Med. *346*, 1513-1521.

Carter, M., Chen, X., Slowinska, B., Minnerath, S., Glickstein, S., Shi, L., Campagne, F., Weinstein, H., and Ross, M.E. (2005). Crooked tail (Cd) model of human folate-responsive neural tube defects is mutated in Wnt coreceptor lipoprotein receptor-related protein 6. Proc. Natl. Acad. Sci. USA *102*, 12843-12848.

Chen, C.N., Chin, K.H., Wang, A.H., and Chou, S.H. (2008). The first crystal structure of gluconolactonase important in the glucose secondary metabolic pathways. J. Mol. Biol. *384*, 604-614.

Chen, V.B., Arendall, W.B., 3rd, Headd, J.J., Keedy, D.A., Immormino, R.M., Kapral, G.J., Murray, L.W., Richardson, J.S., and Richardson, D.C. (2010). MolProbity: all-atom structure validation for macromolecular crystallography. Acta. Crystallogr. D Biol. Crystallogr. *66*, 12-21.

Cheung, W.M., Jin, L.Y., Smith, D.K., Cheung, P.T., Kwan, E.Y., Low, L., and Kung, A.W. (2006). A family with osteoporosis pseudoglioma syndrome due to compound heterozygosity of two novel mutations in the LRP5 gene. Bone *39*, 470-476.

Chufan, E.E., De, M., Eipper, B.A., Mains, R.E., and Amzel, L.M. (2009). Amidation of bioactive peptides: the structure of the lyase domain of the amidating enzyme. Structure *17*, 965-973.

Collins, M.N., and Hendrickson, W.A. (2011). Structural characterization of the Boca/Mesd maturation factors for LDL-receptor-type beta propeller domains. Structure *19*, 324-336.

De Ferrari, G.V., Papassotiropoulos, A., Biechele, T., Wavrant De-Vrieze, F., Avila, M.E., Major, M.B., Myers, A., Saez, K., Henriquez, J.P., Zhao, A.*, et al.* (2007). Common genetic variation within the low-density lipoprotein receptor-related protein 6 and late-onset Alzheimer's disease. Proc. Natl. Acad. Sci. USA *104*, 9434-9439.

Downey, L.M., Bottomley, H.M., Sheridan, E., Ahmed, M., Gilmour, D.F., Inglehearn, C.F., Reddy, A., Agrawal, A., Bradbury, J., and Toomes, C. (2006). Reduced bone mineral density and hyaloid vasculature remnants in a consanguineous recessive FEVR family with a mutation in LRP5. Br. J. Ophthalmol. *90*, 1163-1167.

Edwards, T.A., Wilkinson, B.D., Wharton, R.P., and Aggarwal, A.K. (2003). Model of the brain tumor-Pumilio translation repressor complex. Genes Dev. *17*, 2508-2513.

Emsley, P., and Cowtan, K. (2004). Coot: model-building tools for molecular graphics. Acta Crystallogr. D Biol. Crystallogr. *60*, 2126-2132.

Eswar, N., Webb, B., Marti-Renom, M.A., Madhusudhan, M.S., Eramian, D., Shen, M.Y., Pieper, U., and Sali, A. (2007). Comparative protein structure modeling using MODELLER. Curr. Protoc. Protein Sci. *Chapter 2*, Unit 2.9.

Evans, P. (2006). Scaling and assessment of data quality. Acta Crystallogr. D Biol. Crystallogr. *62*, 72-82.

Fossat, N., Jones, V., Khoo, P.L., Bogani, D., Hardy, A., Steiner, K., Mukhopadhyay, M., Westphal, H., Nolan, P.M., Arkell, R., and Tam, P.P. (2011). Stringent requirement of a proper level of canonical WNT signalling activity for head formation in mouse embryo. Development *138*, 667-676.

Gong, Y., Slee, R.B., Fukai, N., Rawadi, G., Roman-Roman, S., Reginato, A.M., Wang, H., Cundy, T., Glorieux, F.H., Lev, D.*, et al.* (2001). LDL receptor-related protein 5 (LRP5) affects bone accrual and eye development. Cell *107*, 513-523.

Good, M.C., Greenstein, A.E., Young, T.A., Ng, H.L., and Alber, T. (2004). Sensor domain of the Mycobacterium tuberculosis receptor Ser/Thr protein kinase, PknD, forms a highly symmetric beta propeller. J. Mol. Biol. *339*, 459-469.

Gouet, P., Courcelle, E., Stuart, D.I., and Metoz, F. (1999). ESPript: analysis of multiple sequence alignments in PostScript. Bioinformatics *15*, 305-308.

Heymann, J.B., and Belnap, D.M. (2007). Bsoft: image processing and molecular modeling for electron microscopy. J. Struct. Biol. *157*, 3-18.

Holm, L., and Rosenstrom, P. (2010). Dali server: conservation mapping in 3D. Nucl. Acids Res. *38*, W545-549.

Jeon, H., Meng, W., Takagi, J., Eck, M.J., Springer, T.A., and Blacklow, S.C. (2001). Implications for familial hypercholesterolemia from the structure of the LDL receptor YWTD-EGF domain pair. Nat. Struct. Biol. *8*, 499-504.

Jiao, X., Ventruto, V., Trese, M.T., Shastry, B.S., and Hejtmancik, J.F. (2004). Autosomal recessive familial exudative vitreoretinopathy is associated with mutations in LRP5. Am. J. Hum. Genet. *75*, 878-884.

Kabsch, W. (2010). Integration, scaling, space-group assignment and post-refinement. Acta Crystallogr. D Biol. Crystallogr. *66*, 133-144.

Kokubu, C., Heinzmann, U., Kokubu, T., Sakai, N., Kubota, T., Kawai, M., Wahl, M.B., Galceran, J., Grosschedl, R., Ozono, K., and Imai, K. (2004). Skeletal defects in ringelschwanz mutant mice reveal that Lrp6 is required for proper somitogenesis and osteogenesis. Development *131*, 5469-5480.

Krissinel, E., and Henrick, K. (2007). Inference of macromolecular assemblies from crystalline state. J. Mol. Biol. *372*, 774-797.

Larkin, M.A., Blackshields, G., Brown, N.P., Chenna, R., McGettigan, P.A., McWilliam, H., Valentin, F., Wallace, I.M., Wilm, A., Lopez, R.*, et al.* (2007). Clustal W and Clustal X version 2.0. Bioinformatics *23*, 2947-2948.

Lawrence, M.C., and Colman, P.M. (1993). Shape complementarity at protein/protein interfaces. J. Mol. Biol. *234*, 946-950.

Little, R.D., Carulli, J.P., Del Mastro, R.G., Dupuis, J., Osborne, M., Folz, C., Manning, S.P., Swain, P.M., Zhao, S.C., Eustace, B.*, et al.* (2002). A mutation in the LDL receptor-related protein 5 gene results in the autosomal dominant high-bone-mass trait. Am. J. Hum. Genet. *70*, 11-19.

Loftus, S.R., Walker, D., Mate, M.J., Bonsor, D.A., James, R., Moore, G.R., and Kleanthous, C. (2006). Competitive recruitment of the periplasmic translocation portal TolB by a natively disordered domain of colicin E9. Proc. Natl. Acad. Sci. USA *103*, 12353-12358.

Ludtke, S.J., Baldwin, P.R., and Chiu, W. (1999). EMAN: semiautomated software for high-resolution single-particle reconstructions. J. Struct. Biol. *128*, 82-97.

MacDonald, B.T., Yokota, C., Tamai, K., Zeng, X., and He, X. (2008). Wnt signal amplification via activity, cooperativity, and regulation of multiple intracellular PPPSP motifs in the Wnt co-receptor LRP6. J. Biol. Chem. *283*, 16115-16123.

Mani, A., Radhakrishnan, J., Wang, H., Mani, M.A., Nelson-Williams, C., Carew, K.S., Mane, S., Najmabadi, H., Wu, D., and Lifton, R.P. (2007). LRP6 mutation in a family with early coronary disease and metabolic risk factors. Science *315*, 1278-1282.

McCoy, A.J., Grosse-Kunstleve, R.W., Adams, P.D., Winn, M.D., Storoni, L.C., and Read, R.J. (2007). Phaser crystallographic software. J. Appl. Crystallogr. *40*, 658-674.

Murshudov, G.N., Vagin, A.A., and Dodson, E.J. (1997). Refinement of macromolecular structures by the maximum-likelihood method. Acta Crystallogr. D Biol. Crystallogr. *53*, 240-255.

Nikopoulos, K., Venselaar, H., Collin, R.W., Riveiro-Alvarez, R., Boonstra, F.N., Hooymans, J.M., Mukhopadhyay, A., Shears, D., van Bers, M., de Wijs, I.J.*, et al.* (2010). Overview of the mutation spectrum in familial exudative vitreoretinopathy and Norrie disease with identification of 21 novel variants in FZD4, LRP5, and NDP. Hum. Mutat. *31*, 656-666.

Ohi, M., Li, Y., Cheng, Y., and Walz, T. (2004). Negative Staining and Image Classification - Powerful Tools in Modern Electron Microscopy. Biol. Proced. Online *6*, 23-34.

Pangrazio, A., Boudin, E., Piters, E., Damante, G., Iacono, N.L., D'Elia, A.V., Vezzoni, P., Van Hul, W., Villa, A., and Sobacchi, C. (2011). Identification of the first deletion in the LRP5 gene in a patient with Autosomal Dominant Osteopetrosis type I. Bone *49*, 568-571.

Perrakis, A., Morris, R., and Lamzin, V.S. (1999). Automated protein model building combined with iterative structure refinement. Nat. Struct. Biol. *6*, 458-463.

Pettersen, E.F., Goddard, T.D., Huang, C.C., Couch, G.S., Greenblatt, D.M., Meng, E.C., and Ferrin, T.E. (2004). UCSF Chimera--a visualization system for exploratory research and analysis. J. Comput. Chem. *25*, 1605-1612.

Qin, M., Hayashi, H., Oshima, K., Tahira, T., Hayashi, K., and Kondo, H. (2005). Complexity of the genotype-phenotype correlation in familial exudative vitreoretinopathy with mutations in the LRP5 and/or FZD4 genes. Hum. Mutat. *26*, 104-112.

Qin, M., Kondo, H., Tahira, T., and Hayashi, K. (2008). Moderate reduction of Norrin signaling activity associated with the causative missense mutations identified in patients with familial exudative vitreoretinopathy. Hum. Genet. *122*, 615-623.

Rickels, M.R., Zhang, X., Mumm, S., and Whyte, M.P. (2005). Oropharyngeal skeletal disease accompanying high bone mass and novel LRP5 mutation. J. Bone Miner. Res. *20*, 878-885.

Rudenko, G., Henry, L., Henderson, K., Ichtchenko, K., Brown, M.S., Goldstein, J.L., and Deisenhofer, J. (2002). Structure of the LDL receptor extracellular domain at endosomal pH. Science *298*, 2353-2358.

Scheres, S.H., Nunez-Ramirez, R., Sorzano, C.O., Carazo, J.M., and Marabini, R. (2008). Image processing for electron microscopy single-particle analysis using XMIPP. Nat. Protoc. *3*, 977-990.

Semenov, M.V., and He, X. (2006). LRP5 mutations linked to high bone mass diseases cause reduced LRP5 binding and inhibition by SOST. J. Biol. Chem. *281*, 38276-38284.

Streeten, E.A., Beck, T.J., O'Connell, J.R., Rampersand, E., McBride, D.J., Takala, S.L., Pollin, T.I., Uusi-Rasi, K., Mitchell, B.D., and Shuldiner, A.R. (2008). Autosome-wide linkage analysis of hip structural phenotypes in the Old Order Amish. Bone *43*, 607-612.

Stuart, D.I., Levine, M., Muirhead, H., and Stammers, D.K. (1979). Crystal structure of cat muscle pyruvate kinase at a resolution of 2.6 A. J. Mol. Biol. *134*, 109-142.

Takagi, J., Yang, Y., Liu, J.H., Wang, J.H., and Springer, T.A. (2003). Complex between nidogen and laminin fragments reveals a paradigmatic beta-propeller interface. Nature *424*, 969-974.

Tamai, K., Semenov, M., Kato, Y., Spokony, R., Liu, C., Katsuyama, Y., Hess, F., Saint-Jeannet, J.P., and He, X. (2000). LDL-receptor-related proteins in Wnt signal transduction. Nature *407*, 530-535.

Tamai, K., Zeng, X., Liu, C., Zhang, X., Harada, Y., Chang, Z., and He, X. (2004). A mechanism for Wnt coreceptor activation. Mol. Cell. *13*, 149-156.

Toomes, C., Bottomley, H.M., Jackson, R.M., Towns, K.V., Scott, S., Mackey, D.A., Craig, J.E., Jiang, L., Yang, Z., Trembath, R.*, et al.* (2004). Mutations in LRP5 or FZD4 underlie the common familial exudative vitreoretinopathy locus on chromosome 11q. Am. J. Hum. Genet. *74*, 721-730.

Van Wesenbeeck, L., Cleiren, E., Gram, J., Beals, R.K., Benichou, O., Scopelliti, D., Key, L., Renton, T., Bartels, C., Gong, Y.*, et al.* (2003). Six novel missense mutations in the LDL receptor-related protein 5 (LRP5) gene in different conditions with an increased bone density. Am. J. Hum. Genet. *72*, 763-771.

Walter, T.S., Diprose, J.M., Mayo, C.J., Siebold, C., Pickford, M.G., Carter, L., Sutton, G.C., Berrow, N.S., Brown, J., Berry, I.M.*, et al.* (2005). A procedure for setting up high-throughput nanolitre crystallization experiments. Crystallization workflow for initial screening, automated storage, imaging and optimization. Acta Crystallogr. D Biol. Crystallogr. *61*, 651-657.